Check for updates

Cathodic shift of a photo-potential on a Ta₃N₅ photoanode by post-heating a TiO₂ passivation layer†

Jie Liu,[a] Wenjun Luo, [ID] *[a] Kaijian Zhu,[a] Xin Wen,[b] Fei Xiu,[a] Jiajie Yuan,[a] Zhigang Zou[b] and Wei Huang*[ac]

Ta₃N₅ is a promising photoanode material for solar water splitting due to its suitable band gap and high theoretical solar energy conversion. A high onset potential of Ta₃N₅ limits its photoelectrochemical performance due to serious surface charge recombination. In a previous study, a TiO₂ passivation layer was usually coated on the surface of Ta₃N₅ to reduce the surface recombination and improve the performance of a sample. However, to date, there are no studies on the effect of conductivity of the TiO₂ passivation layer on the photoelectrochemical properties of a Ta₃N₅ photoanode. In this work, for the first time, the conductivity of TiO₂ is increased by post-heating of a TiO₂ passivation layer, leading to a 90 mV cathodic shift of the photo-potential of Ta₃N₅. After further loading with a Ni(OH)$_x$/FeOOH bi-layer electrocatalyst, the Ta₃N₅ photoanode achieves a current density of 6.4 mA cm^{-2} at 1.23 V$_{RHE}$ and a HC-STH (half-cell solar to hydrogen efficiency) of 0.72% under a sunlight simulator (100 mW cm^{-2}), which are the highest values among the Ta₃N₅ photoanodes prepared by thermal oxidation and nitridation of Ta foil.

1. Introduction

Since Fujishima and Honda reported the use of a TiO₂ photo-anode to split water into H₂ and O₂ under illumination,[1] solar water splitting has become a promising method to convert solar energy into clean and high energy density H₂.[2,3] In the past forty years, three kinds of photoelectrochemical (PEC) cells, including PV (photovoltaic) + electrolysis, PV + PEC and a p–n tandem cell, have been explored.[4–9] In a p–n tandem cell, a n-type semiconductor as a photoanode is ohmically contacted with a p-type semiconductor as a photocathode. A two-photon system is used to split water in a p–n tandem cell and has higher efficiency than that of a conventional single-photon cell. Moreover, no expensive PV cells are used. Therefore, a p–n tandem cell is the most promising one due to its high theoretical efficiency and low cost.[10,11]

Recently, some n-type semiconductors, BiVO₄, Fe₂O₃ and Ta₃N₅, have been intensively studied as photoanodes.[12–15] The band gap of BiVO₄ is too wide (2.4 eV), which leads to a low theoretical efficiency (9.1%), even lower than the minimum efficiency (10%) for practical applications.[12] Though Fe₂O₃ has a high theoretical efficiency (16%), most of the samples achieve photocurrent lower than 4 mA cm^{-2}, which leads to an experimental efficiency lower than 5%.[16,17] The low efficiency is due to an intrinsic short hole diffusion length caused by a local d-band composition in valence band of Fe₂O₃.[18] In 2002, Ta₃N₅ was firstly reported as a visible light photocatalyst for water splitting by Domen's group.[19] Though Ta₃N₅ has a similar band gap (2.1 eV) and theoretical photocurrent with Fe₂O₃, a valence band of Ta₃N₅ is composed of N2p and has a longer hole diffusion length than that of Fe₂O₃. Moreover, the bottom of conduction band of Ta₃N₅ is at −0.3 V$_{RHE}$, 0.6 V higher than that of Fe₂O₃, which means a more negative onset potential and a lower bias for photoelectrochemical water oxidation.[20,21] Therefore, it is easier for a Ta₃N₅ photoanode to obtain high efficiency than Fe₂O₃. In recent years, photocurrent of Ta₃N₅ has been boosted to a theoretical maximum value.[14,22–24] However, an onset potential of a Ta₃N₅ photoanode (0.6–0.8 V$_{RHE}$) is still much positive than the theoretical value (−0.3 V$_{RHE}$) even after coating efficient electrocatalysts on the surface of Ta₃N₅ to accelerate interface charge transfer.[22,25–27] The positive onset potential of a Ta₃N₅ photoanode mainly originates from poor bulk transport of majority carriers and severe surface carrier recombina-tion.[14,28,29] In order to further lower an onset potential, a TiO₂

[a]Key Laboratory of Flexible Electronics (KLOFE), Institute of Advanced Materials (IAM), Jiangsu National Synergetic Innovation Center for Advanced Materials (SICAM), Nanjing Tech University (Nanjing Tech), 30 South Puzhu Road, Nanjing 211816, P. R. China. E-mail: iamwjluo@njtech.edu.cn; iamwhuang@njtech.edu.cn

[b]Eco-materials and Renewable Energy Research Center (ERERC), National Laboratory of Solid State Microstructures, Department of Physics, Nanjing University, Nanjing 210093, P. R. China

[c]Key Laboratory for Organic Electronics & Information Displays (KLOEID), Institute of Advanced Materials (IAM), Nanjing University of Posts and Telecommunications, Wenyuan Road 9, Nanjing 210023, China

† Electronic supplementary information (ESI) available. See DOI: 10.1039/c7ra04647b

surface passivation layer was coated on the surface of Ta_3N_5 because TiO_2 could reduce surface recombination of photo-generated carriers.[30–33] However, to date, there are few studies on effect of conductivity of the TiO_2 passivation layer on photoelectrochemical property of a Ta_3N_5 photoanode.

In this study, we found that the large amount of OH^- group exist in an as-deposited TiO_2 passivation layer to form $TiO_x(OH)_y$, which impeded interface hole transfer and limited a conversion efficiency of Ta_3N_5. A strategy of post-heating of TiO_2 passivation layer was proposed to cathodically shift photopotential of Ta_3N_5 by about 90 mV. After post-heating at a low temperature, $TiO_x(OH)_y$ in the as-deposited passivation layer was dehydrated into $TiO_x(OH)_{y-\delta}$, which enhanced the interface hole transfer. Therefore, an onset potential of a Ta_3N_5 photoanode was cathodically shifted. To the best of our knowledge, it is the first time to shift the onset potential of Ta_3N_5 by heating a TiO_2 passivation layer at a low temperature. This strategy not only deepens understanding the role of a TiO_2 passivation layer in a photoelectrochemical cell but also offers reference to improve the performance of other photoelectrodes.

2. Experimental section

2.1 Preparation of Ta_3N_5 photoanodes

Ta_3N_5 photoanodes were prepared by modified oxidation and nitridation of Ta foils at a high temperature.[14] Ta foils (7 × 16 mm) were firstly rinsed by isopropanol, acetone and ethanol before use, respectively. In order to remove the oxygen-rich surface recombination layer, Ta foils were etched in 5 mL hydrofluoric acid solution (40%) for 225 min at room temperature (25 °C), and then rinsed with distilled water and ethanol. The etched Ta foils were calcined in air at 554 °C for 30 min to obtain Ta_2O_5 film, followed by a further nitridation treatment under a flow of ammonia gas (800 mL min^{-1}) at 900 °C for 8 h to become Ta_3N_5. A Ta foil without etching was also calcined in the same conditions as a reference to investigate the etching effect.

2.2 Deposition of a TiO_2 passivation layer

A TiO_2 passivation layer was deposited by CBD method.[24] 200 μL of titanium trichloride solution (20%) was added into 20 mL of deionized water in ice water bath. A Ta_3N_5 sample was vertically immersed into the obtained solution, and a TiO_2 passivation layer was deposited on the surface of a Ta_3N_5 sample at 70 °C for 6 min. After washed with distilled water, the TiO_2 coated Ta_3N_5 electrode was calcined in nitrogen atmosphere at different temperatures (100 °C, 150 °C, 200 °C, and 250 °C) for 30 min in a tube furnace. A TiO_2 coated Ta_3N_5 electrode without calcination was also prepared as a reference.

2.3 Coating of a $Ni(OH)_x$/FeOOH bi-layer electrocatalyst

A FeOOH layer and a $Ni(OH)_x$ layer were deposited on a TiO_2 coated Ta_3N_5 photoelectrode by CBD method and electro-deposition method,[24] respectively. A FeOOH layer was deposited in a mixture of 50 mM $Fe(NO)_3$ and 500 mM $NaNO_3$ aqueous solution at 100 °C for 20 min. After washed with distilled water and dried in air, a $Ni(OH)_x$ layer was electro-

deposited with a potential of −0.85 V vs. saturated calomel electrode (SCE) in 0.1 M $NiSO_4$ aqueous solution at room temperature. The deposition charge was about 12 mC cm^{-2}.

2.4 Characterization of samples

The crystal structures of samples were measured by X-ray diffraction patterns (XRD, Bruker D8 ADVANCE diffractometer). The morphologies of samples were observed by field-emission scanning electron microscopy (FE-SEM, Nova Nano-SEM 230, FEI). XPS spectra of samples were obtained by using a Thermo ESCALAB 250 machine and the binding energy was calibrated by C1s (284.8 eV).

2.5 Photoelectrochemical measurement

The photoelectrochemical properties were conducted in an electrochemical analyzer (CHI-660D, Shanghai Chenhua). A Ta_3N_5 electrode, SCE and Pt foil were used as the working electrode, reference electrode and counter electrode, respectively. 1 M NaOH (pH = 13.6) aqueous solution was used as electrolyte. A reversible hydrogen electrode (RHE) potential was obtained by the formula:

$$E(V \text{ vs. RHE}) = E(V \text{ vs. SCE}) + 0.242V + 0.059 \times pH$$

A Xe lamp and AM 1.5G sunlight simulator (100 mW cm^{-2}, Newport oriel 92251A-1000) were used as light sources, respectively. The electrochemical impedance spectra (EIS) of samples were measured by an electrochemical analyzer (Solartron1260 + 1287) with a 10 mV amplitude perturbation and frequencies between 0.1 Hz and 10 MHz. The incident photon-to-current efficiency (IPCE) was measured under irradiation of different wavelengths of light generated by monochromatic filters. A photometer (Newport, 840-C, USA) was used to detect light intensity. The IPCE was calculated as follow:

$$IPCE = 1240 \times I_{ph}/P\lambda$$

where I_{ph} is photocurrent density (μA cm^{-2}), P and λ are incident light intensity (μW cm^{-2}) and wavelength (nm), respectively.

3. Results and discussion

3.1 Improved efficiency of Ta_3N_5 by etching a Ta foil precursor with HF solution

In our previous study, a smooth and thin layer of Ta_3N_5 with high oxygen impurity existed on the surface of an as-prepared sample, which played a role as surface recombination center and lowered the conversion efficiency of Ta_3N_5. By removing the Ta_3N_5 surface layer through thermal or mechanical exfoliation method, an efficient Ta_3N_5 photoanode was obtained.[14] In this study, a new surface etching approach was carried out on a Ta foil precursor with HF aqueous solution before oxidation and nitridation. The oxidation temperature was 554 °C, lower than the critical temperature of 590 °C.[14] Therefore, no surface thermal exfoliation was observed on the Ta_3N_5 samples in this study. Fig. 1a and b shows SEM images of Ta_3N_5 from Ta foil
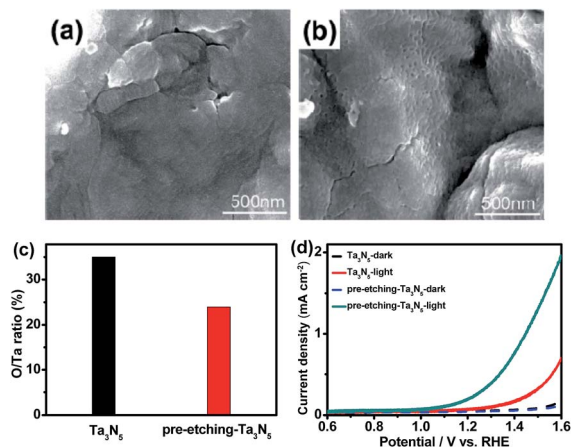
Fig. 1 SEM images of Ta$_3$N$_5$ from Ta foil precursor without (a) and with (b) surface etching; (c) O/Ta ratios on the surface of Ta$_3$N$_5$ by XPS from a Ta foil precursor with and without surface etching; (d) current–potential curves of Ta$_3$N$_5$ photoanodes from Ta foil precursor with and without surface etching in 1 M NaOH aqueous solution (pH = 13.6) under xenon lamp irradiation.

Fig. 2 (a) Current–potential curves of Ta$_3$N$_5$/F/N, Ta$_3$N$_5$/TiO$_2$ (25 °C)/ F/N, Ta$_3$N$_5$/TiO$_2$ (100 °C)/F/N, Ta$_3$N$_5$/TiO$_2$ (150 °C)/F/N, Ta$_3$N$_5$/TiO$_2$ (200 °C)/F/N, Ta$_3$N$_5$/TiO$_2$ (250 °C)/F/N and Ta$_3$N$_5$ (200 °C)/F/N without TiO$_2$ in 1 M NaOH (pH = 13.6) under 300 W xenon lamp irradiation; (b) photo-potentials@1.5 mA cm^{-2} of the samples vs. post-heating temperatures; (c) current density–time curves of Ta$_3$N$_5$/TiO$_2$ (25 °C)/F/N and Ta$_3$N$_5$/TiO$_2$ (200 °C)/F/N at 1.23 V$_{RHE}$ under 300 W xenon lamp irradiation.

precursor without and with surface etching, respectively. Without surface etching, a smooth surface is observed on the sample. The surface becomes rougher after surface etching of Ta foil precursor and some particles, aggregates and grooves are observed. XRD (see Fig. S1a and Table S1†) and Raman (see Fig. S1b†) results suggest that there are no obvious differences in crystal structures and grain sizes between the two samples before and after etching. XPS indicates the ratio of O/Ta on the surface of Ta$_3$N$_5$ decreases from 0.35 to 0.24 after surface etching of Ta foil precursor (see Fig. 1c). The surface etching of Ta foil precursor with HF solution is a new method to remove an oxygen-rich surface layer. Fig. 1d indicates photoelectrochemical properties of Ta$_3$N$_5$ photoanodes from Ta foils with and without surface etching. After surface etching, the performance of a Ta$_3$N$_5$ photoanode increases remarkably, which comes from the surface oxygen-rich layer removal. The result is in good agreement with our previous study.

3.2 Effect of post-heating a TiO$_2$ passivation layer on a photo-potential of a Ta$_3$N$_5$ photoanode

Efficient Ni(OH)$_x$/FeOOH bilayer electrocatalysts for OER were coated on the surface of Ta$_3$N$_5$ photoanodes to accelerate the water oxidation process, following a previous report.[24] In this study, a Ni(OH)$_x$/FeOOH coated Ta$_3$N$_5$ sample is referred as Ta$_3$N$_5$/F/N. In order to further decrease the surface recombination of Ta$_3$N$_5$, post-heating a TiO$_2$ passivation layer in nitrogen atmosphere at different temperatures was carried out. Fig. 2a indicates photoelectrochemical properties of Ta$_3$N$_5$/TiO$_2$/F/N after post-heating TiO$_2$ at different temperatures, and Ta$_3$N$_5$/F/N references without a TiO$_2$ layer before and after calcining at 200 °C. After coating a TiO$_2$ passivation layer, an onset potential of Ta$_3$N$_5$/F/N shifts cathodically, which is in good agreement with previous study.[31] However, in previous studies,[24,31] no post-treatment of a TiO$_2$ passivation layer was
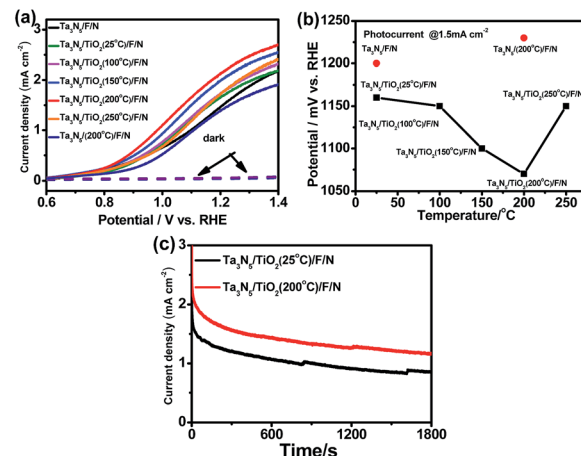
carried out to further improve the performance of a Ta$_3$N$_5$ photoanode. In this study, after post-heating a TiO$_2$ passivation layer in N$_2$ at different temperatures for 30 min, the onset potential of Ta$_3$N$_5$/F/N with a TiO$_2$ passivation layer is cathodically shifted. The optimized post-heating temperature is 200 °C. Compared to the sample post-heating at 200 °C, an onset potential of Ta$_3$N$_5$/TiO$_2$/F/N with post-heating at 250 °C is anodic shifted. An onset potential of Ta$_3$N$_5$/F/N without a TiO$_2$ passivation layer is also anodic shifted after post-heating Ta$_3$N$_5$ in N$_2$ at 200 °C for the same time. The results suggest that the cathodic shift of onset potentials of Ta$_3$N$_5$/F/N with a TiO$_2$ passivation layer after post-heating does not come from post-heating Ta$_3$N$_5$, but the TiO$_2$ passivation layer.

Fig. 2b shows the photo-potential (@1.5 mA cm^{-2}) of the samples with post-heating TiO$_2$ at different temperatures. After coating a TiO$_2$ passivation layer at room temperature, a photo-potential of a Ta$_3$N$_5$/F/N is cathodically shifted about 40 mV. An photo-potential is further cathodically shifted about 10 mV, 60 mV and 90 mV after post-heating TiO$_2$ passivation layers at 100 °C, 150 °C and 200 °C, respectively. Two kinds of slopes of photo-potential decrease are observed at the post-heating temperature lower and higher than 100 °C, suggesting 100 °C is a critical temperature to activate the TiO$_2$ passivation layer. When the post-heating temperature is increased to 250 °C, a photo-potential is anodically shifted about 50 mV, which comes from decreased performance of a Ta$_3$N$_5$ photoanode after post-heated at such a high temperature. The result suggests that the improved performance of a TiO$_2$ coated Ta$_3$N$_5$ comes from the post-heating treatment of TiO$_2$ but not Ta$_3$N$_5$. Fig. 2c indicates the photo-stability of Ta$_3$N$_5$/TiO$_2$/F/N with and without post-heating TiO$_2$ at 200 °C. Photo-stability of the two samples is similar and the increased photocurrent can be kept during 1800s' illumination, suggesting that the post-heating treatment makes Ta$_3$N$_5$/TiO$_2$/F/N change irreversibly.

3.3 A mechanism for improved performance of a Ta_3N_5 photoanode by post-heating a TiO_2 passivation layer

Fig. 3 indicates surface morphologies of Ta_3N_5, Ta_3N_5/TiO_2 (25 °C), Ta_3N_5/TiO_2 (200 °C) and Ta_3N_5/TiO_2 (200 °C)/F/N, respectively. Some pores are observed on the surface of Ta_3N_5, which comes from decreased quantity of anions after nitriding Ta_2O_5 into Ta_3N_5.[34] No obvious morphology change is observed after coating and post-heating a TiO_2 passivation layer at 200 °C, which suggests that the TiO_2 layer is very thin (Fig. 3b and c), several nanometer, according to previous study.[24] After loading a $Ni(OH)_x$/FeOOH bilayer electrocatalyst, some nanoparticles uniformly distribute on the surface of a Ta_3N_5 photoanode (see Fig. 3d). X-ray diffraction patterns (XRD) and Raman was also employed to characterize TiO_2 on the surface of Ta_3N_5 samples with post-heating TiO_2 at different temperatures (see Fig. S3 and S4†). All the samples show the same XRD and Raman patterns with a bare Ta_3N_5 sample and no TiO_2's signal is observed possibly due to the thin and poor crystalline of a TiO_2 layer.

Fig. 4a and b show XPS peaks of Ta4f and N1s in TiO_2 coated Ta_3N_5 samples at different post-heating temperatures, respectively. Binding energies of Ta4f (25.2 eV and 27.1 eV) in Fig. 4a are assigned to Ta^{5+} in a TiO_2 coated Ta_3N_5 without post-heating, which do not shift after post-heating at temperatures of 100 °C, 150 °C and 200 °C. However, the binding energies shift to lower values about 0.1 eV after post-heating at 250 °C. Fig. 4b indicates similar trend of N1s with that in Fig. 4a. The results suggest that the valence state of Ta^{5+} and N^{3-} in Ta_3N_5 did not change when post-heating at a temperature lower than 200 °C. However, Ta_3N_5 is oxidized during post-heating at 250 °C due to residual O_2 impurity in N_2 carrier gas.[35,36] The binding energies of Ti2p (465 eV and 459 eV) in Fig. 4c are assigned to Ti^{4+},[37,38] which shift to lower binding energy as post-heating temperatures increase. The peak shift possibly comes from dehydration of titanium hydroxides into TiO_x at high temperatures.[38]

Fig. 5a shows the XPS spectra of O1s in the Ta_3N_5/TiO_2 at different post-heating temperatures. Three kinds of peaks
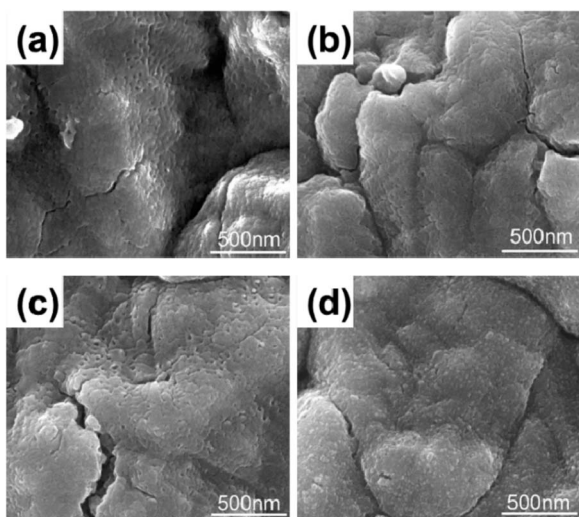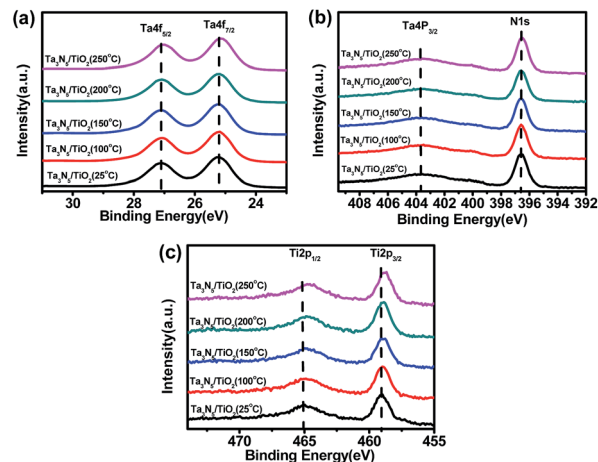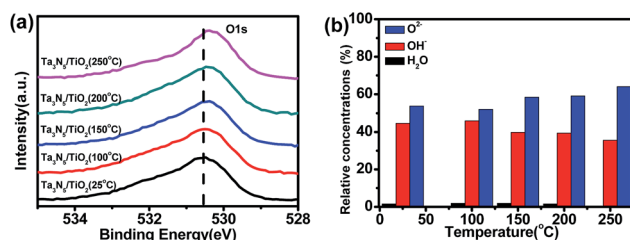
Fig. 4 XPS spectra of (a) Ta4f$_{5/2}$ and Ta4f$_{7/2}$, (b) Ta4p$_{3/2}$ and N1s, (c) Ti2p$_{1/2}$ and Ti2p$_{3/2}$ of Ta_3N_5/TiO_2 (25 °C), Ta_3N_5/TiO_2 (100 °C), Ta_3N_5/TiO_2 (150 °C), Ta_3N_5/TiO_2 (200 °C), Ta_3N_5/TiO_2 (250 °C).

(c)Sample	OH$^-$/O^{2-}
Ta_3N_5/TiO_2(25°C)	0.83
Ta_3N_5/TiO_2(100°C)	0.88
Ta_3N_5/TiO_2(150°C)	0.68
Ta_3N_5/TiO_2(200°C)	0.66
Ta_3N_5/TiO_2(250°C)	0.55

Fig. 5 (a) XPS spectra of O1s (b) relative concentrations of adsorbed H_2O (dark), lattice OH$^-$ (red), lattice O^{2-} (blue) vs. post-heating temperatures and (c) ratio of OH$^-$ to O^{2-} on the surface of Ta_3N_5/TiO_2 (25 °C), Ta_3N_5/TiO_2 (100 °C), Ta_3N_5/TiO_2 (150 °C), Ta_3N_5/TiO_2 (200 °C), Ta_3N_5/TiO_2 (250 °C).

(530.4 eV, 531.5 eV and 533.5 eV) are used to fit XPS spectra of O1s, which are assigned to lattice O^{2-}, lattice OH^- and adsorbed H_2O (see Fig. S5†), respectively.[39,40] The relative concentrations of these three kinds of oxygen species are calculated from XPS data and the results are shown in Fig. 5b. The ratio of OH^- to O^{2-} in the sample without post-heating is 0.83, which does not change obviously after post-heating at 100 °C, and decreases to 0.55 when the calcination temperature is 250 °C (see Fig. 5c). The OH^- content of the samples decreases with higher post-heating temperature, due to the dehydration reaction during the post-heating process:[41] Ti-OH + HO-Ti → Ti–O–Ti + H_2O. Therefore, the post-heating of a TiO_2 coated Ta_3N_5 leads to a reduction of OH^- content in the TiO_2 passivation layer. However, when the post-heating temperature is lower than

Fig. 3 Surface SEM images of (a) Ta_3N_5, (b) Ta_3N_5/TiO_2 (25 °C), (c) Ta_3N_5/TiO_2 (200 °C), (d) Ta_3N_5/TiO_2 (200 °C)/F/N.

100 °C, no OH⁻ decrease is observed. These results suggest that there is a barrier for the dehydration reaction.

In order to understand the effect of post-heating on photo-potential of a TiO$_2$ coated Ta$_3$N$_5$, electrochemical impedance spectroscopy (EIS) measurement of the samples was also carried out and the results are shown in Fig. 6a. An equivalent circuit is plotted in the inset of Fig. 6a. R_{ct}, R_s, and CPE represent a charge transfer resistance in semiconductor–electrolyte interface, an electrolyte resistance and a constant phase element of a double layer, respectively.[31] The semicircle of a TiO$_2$ coated Ta$_3$N$_5$ with post-heating at 200 °C is the smallest, indicating a fastest interface charge transfer speed among the five samples. Fig. 6b shows the R_{ct} values of the TiO$_2$ coated Ta$_3$N$_5$ samples with post-heating at different temperatures. There is a positive correlation between the performance of a TiO$_2$ coated Ta$_3$N$_5$ and interface charge transfer. Therefore, reduced OH⁻ content in the TiO$_2$ passivation layer after the post-heating process, which leads to an increase of interface charge transfer and cathodic shift of the photo-potential.

Photocurrent–potential curves of Ta$_3$N$_5$ before and after depositing TiO$_2$ layer in 1 M NaOH with H$_2$O$_2$ as sacrificial reagent were measured and the results are shown in Fig. S6a.† From Fig. S6a,† the photocurrent of Ta$_3$N$_5$ in the solution with sacrificial reagent are similar to the samples after depositing a TiO$_2$ layer and post-heating TiO$_2$ layer, which suggests that charge separation efficiency does not change after depositing the TiO$_2$ layer.[15] Therefore, the improved performance of a TiO$_2$ coated Ta$_3$N$_5$ photoanode for water oxidation comes from enhanced interfacial charge transfer efficiency, which is in agreement with previous study.[24] Both loading oxygen evolution reaction (OER) catalysts and passivating surface defect states by noncatalysts can enhance interfacial charge transfer efficiency.[42] In order to investigate the role of a TiO$_2$ layer, current–potential curves of FTO, FTO/TiO$_2$ and FTO/TiO$_2$ (200 °C) for oxygen evolution reaction are shown in Fig. S6b.† The OER current of FTO decreases after depositing a TiO$_2$ layer, whether post-heating or not. The results suggest that no catalysis effects are observed on the TiO$_2$ layer, which are in good agreement with previous studies.[24,32,33] Therefore, the TiO$_2$ layer plays a role as a passivation layer,[31,43] which reduces the surface carrier recombination and facilitate interfacial charge transfer.

According to XPS and EIS results, a mechanism of cathodic shift photo-potential after post-heating a TiO$_2$ layer is illustrated in Fig. 7. Before post-heating, holes are generated in the
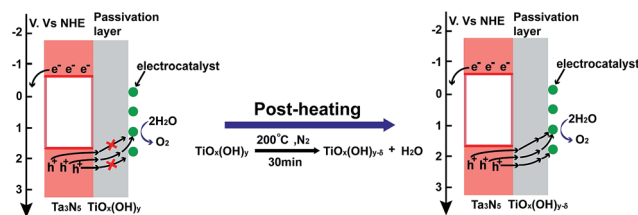

Fig. 7 Illustration of energy band positions and interface charge transfer in a TiO$_2$ coated Ta$_3$N$_5$ before and after post-heating.

valence band of Ta$_3$N$_5$, which transfer to the TiO$_2$ passivation layer and then to electrocatalysts for water oxidation under illumination. From EIS in Fig. 6, large amount of OH⁻ in the as-deposited TiO$_2$ decreases conductivity of TiO$_2$ and limits hole transfer in the TiO$_2$ passivation layer. After post-heating, OH⁻ content in TiO$_2$ decrease and increase the conductivity of the passivation layer. Therefore, hole transfer in a TiO$_2$ passivation layer is increased after post-heating. However, if the post-heating temperature is too high (250 °C), Ta$_3$N$_5$ can be oxidized and the performance of the samples becomes lower. Therefore, an optimum post-heating temperature is observed.

3.4 Performance of a Ta$_3$N$_5$ photoanode with post-heating a TiO$_2$ passivation layer under sunlight simulator illumination

Fig. 8a shows current–potential curves of the Ta$_3$N$_5$/TiO$_2$ (200 °C)/F/N under a standard measurement condition to compare the performance of our sample with previous studies. A photocurrent of 6.4 mA cm⁻² at 1.23 V$_{RHE}$ is achieved in the Ta$_3$N$_5$/TiO$_2$ (200 °C)/F/N. The IPCEs at 1.23 V$_{RHE}$ of the samples were measured and the results are shown in Fig. 8b. An integrated photocurrent is calculated as 6.2 mA cm⁻² from IPCEs at the standard solar spectrum, which is consistent with the measured value in Fig. 8a. Therefore, the solar photocurrent in
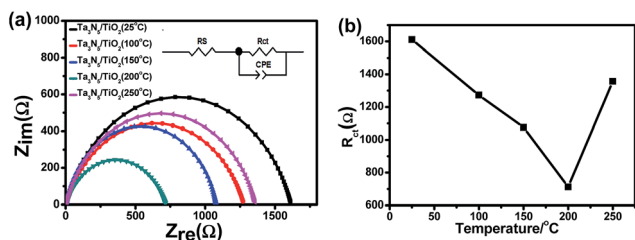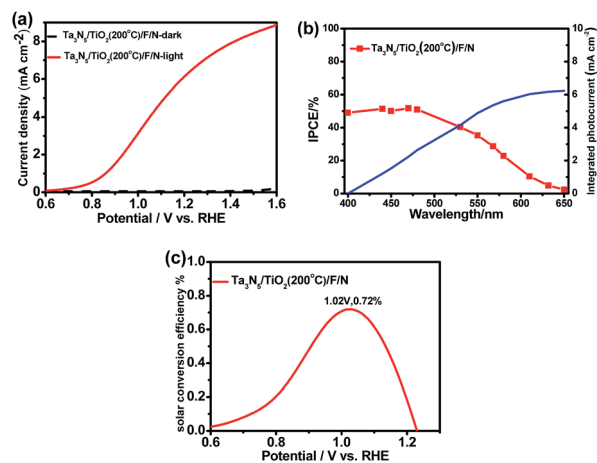

Fig. 8 (a) A current–potential curve of Ta$_3$N$_5$/TiO$_2$ (200 °C)/F/N photoanode and (b) the corresponding IPCEs at 1.23 V$_{RHE}$; (c) a half-cell solar to hydrogen efficiency electrolyte: 1 M NaOH (pH = 13.6), light source: AM 1.5G simulated sunlight (100 mW cm⁻²).

Fig. 6 (a) EIS of Ta$_3$N$_5$/TiO$_2$ (25 °C), Ta$_3$N$_5$/TiO$_2$ (100 °C), Ta$_3$N$_5$/TiO$_2$ (150 °C), Ta$_3$N$_5$/TiO$_2$ (200 °C), Ta$_3$N$_5$/TiO$_2$ (250 °C); (b) interface charge transfer resistance R_{ct} vs. post-heating temperatures.

Fig. 8a is reliable. A half-cell solar to hydrogen efficiency (HC-STH) is calculated as 0.72% at 1.02 V_{RHE} (Fig. 8c). The photocurrent at 1.23 V_{RHE} and HC-STH are the highest values among Ta_3N_5 photoanodes prepared by oxidation and nitridation of Ta foils method. The results suggest that post-heating is an effective strategy to obtain efficient TiO_2 coated Ta_3N_5 photoanodes for solar water splitting.

4.   Conclusion

In summary, a new etching method was used to remove an oxygen-rich surface layer of Ta_3N_5 and enhanced the performance of a Ta_3N_5 photoanode. The conversion efficiency of Ta_3N_5 was improved by coating a TiO_2 passivation layer on the surface. We found that amount of OH^- decreased the conductivity of an as-deposited TiO_2 layer, which limited the performance of a TiO_2 coated Ta_3N_5. Therefore, a post-heating treatment was proposed to decrease OH^- species and increase the conductivity of TiO_2, which cathodically shifted the photopotential of Ta_3N_5 about 90 mV. After the post-heating, a photocurrent of 6.4 mA cm^{-2} at 1.23 V_{RHE} and a HC-STH efficiency of 0.72% were obtained in a TiO_2 coated Ta_3N_5 photoanode with $Ni(OH)_x$/FeOOH bilayer electrocatalyst, which are the highest values among Ta_3N_5 photoanodes prepared by thermal oxidation and nitridation of Ta foils.

Acknowledgements

Notes and references

1 A. Fujishima and K. Honda, *Nature*, 1972, **238**, 37–38.

2 M. Gratzel, *Nature*, 2001, **414**, 338–344.

3 M. G. Walter, E. L. Warren, J. R. McKone, S. W. Boettcher, Q. Mi, E. A. Santori and N. S. Lewis, *Chem. Rev.*, 2010, **110**, 6446–6473.

4 O. Khaselev, A. Bansal and J. A. Turner, *Int. J. Hydrogen Energy*, 2001, **26**, 127–132.

5 M. C. Hanna and A. J. Nozik, *J. Appl. Phys.*, 2006, **100**, 074510.

6 O. Khaselev and J. A. Turner, *Science*, 1998, **280**, 425–427.

7 K. Ohashi, J. McCann and J. O. M. Bockris, *Nature*, 1977, **266**, 610–611.

8 J. Akikusa and S. U. M. Khan, *Int. J. Hydrogen Energy*, 2002, **27**, 863–870.

9 A. J. Nozik, *Appl. Phys. Lett.*, 1976, **29**, 150–153.

10 L. Fornarini, A. J. Nozik and B. A. Parkinson, *J. Phys. Chem.*, 1984, **88**, 3238–3243.

11 M. S. Prévot and K. Sivula, *J. Phys. Chem. C*, 2013, **117**, 17879–17893.

12 W. Luo, Z. Yang, Z. Li, J. Zhang, J. Liu, Z. Zhao, Z. Wang, S. Yan, T. Yu and Z. Zou, *Energy Environ. Sci.*, 2011, **4**, 4046–4051.

13 D. P. Cao, W. J. Luo, J. Y. Feng, X. Zhao, Z. S. Li and Z. G. Zou, *Energy Environ. Sci.*, 2014, **7**, 752–759.

14 M. Li, W. Luo, D. Cao, X. Zhao, Z. Li, T. Yu and Z. Zou, *Angew. Chem., Int. Ed.*, 2013, **52**, 11016–11020.

15 Z. Li, W. Luo, M. Zhang, J. Feng and Z. Zou, *Energy Environ. Sci.*, 2013, **6**, 347–370.

16 S. D. Tilley, M. Cornuz, K. Sivula and M. Graetzel, *Angew. Chem., Int. Ed.*, 2010, **49**, 6405–6408.

17 S. C. Warren, K. Voitchovsky, H. Dotan, C. M. Leroy, M. Cornuz, F. Stellacci, C. Hebert, A. Rothschild and M. Graetzel, *Nat. Mater.*, 2013, **12**, 842–849.

18 M. N. Huda, A. Walsh, Y. Yan, S.-H. Wei and M. M. Al-Jassim, *J. Appl. Phys.*, 2010, **107**, 123712.

19 G. Hitoki, A. Ishikawa, T. Takata, J. N. Kondo, M. Hara and K. Domen, *Chem. Lett.*, 2002, **7**, 736–737.

20 C. M. Fang, E. Orhan, G. A. de Wijs, H. T. Hintzen, R. A. de Groot, R. Marchand, J. Y. Saillard and G. de With, *J. Mater. Chem.*, 2001, **11**, 1248–1252.

21 W. J. Chun, A. Ishikawa, H. Fujisawa, T. Takata, J. N. Kondo, M. Hara, M. Kawai, Y. Matsumoto and K. Domen, *J. Phys. Chem. B*, 2003, **107**, 1798–1803.

22 Y. Li, L. Zhang, A. Torres-Pardo, J. M. Gonzalez-Calbet, Y. Ma, P. Oleynikov, O. Terasaki, S. Asahina, M. Shima, D. Cha, L. Zhao, K. Takanabe, J. Kubota and K. Domen, *Nat. Commun.*, 2013, **4**, 2566.

23 L. Wang, X. Zhou, N. T. Nguyen, I. Hwang and P. Schmuki, *Adv. Mater.*, 2016, **28**, 2432–2438.

24 G. Liu, S. Ye, P. Yan, F. Xiong, P. Fu, Z. Wang, Z. Chen, J. Shi and C. Li, *Energy Environ. Sci.*, 2016, **9**, 1327–1334.

25 M. Liao, J. Feng, W. Luo, Z. Wang, J. Zhang, Z. Li, T. Yu and Z. Zou, *Adv. Funct. Mater.*, 2012, **22**, 3066–3074.

26 G. Liu, J. Shi, F. Zhang, Z. Chen, J. Han, C. Ding, S. Chen, Z. Wang, H. Han and C. Li, *Angew. Chem., Int. Ed.*, 2014, **53**, 7295–7299.

27 L. Wang, F. Dionigi, N. Nhat Truong, R. Kirchgeorg, M. Gliech, S. Grigorescu, P. Strasser and P. Schmuki, *Chem. Mater.*, 2015, **27**, 2360–2366.

28 C. Wang, T. Hisatomi, T. Minegishi, M. Nakabayashi, N. Shibata, M. Katayama and K. Domen, *J. Mater. Chem. A*, 2016, **4**, 13837–13843.

29 E. Nurlaela, S. Ould-Chikh, M. Harb, S. del Gobbo, M. Aouine, E. Puzenat, P. Sautet, K. Domen, J.-M. Basset and K. Takanabe, *Chem. Mater.*, 2014, **26**, 4812–4825.

30 S. Hu, M. R. Shaner, J. A. Beardslee, M. Lichterman, B. S. Brunschwig and N. S. Lewis, *Science*, 2014, **344**, 1005–1009.

31 P. Zhang, T. Wang and J. Gong, *Chem. Commun.*, 2016, **52**, 8806–8809.

32 X. Yang, R. Liu, C. Du, P. Dai, Z. Zheng and D. Wang, *ACS Appl. Mater. Interfaces*, 2014, **6**, 12005–12011.

33 M. G. Ahmed, I. E. Kretschmer, T. A. Kandiel, A. Y. Ahmed, F. A. Rashwan and D. W. Bahnemann, *ACS Appl. Mater. Interfaces*, 2015, **7**, 24053–24062.

34 B. A. Pinaud, P. C. K. Vesborg and T. F. Jaramillo, *J. Phys. Chem. C*, 2012, **116**, 15918–15924.

35 A. Ishikawa, T. Takata, J. N. Kondo, M. Hara and K. Domen, *J. Phys. Chem. B*, 2004, **108**, 11049–11053.

36 D. Yokoyama, H. Hashiguchi, K. Maeda, T. Minegishi, T. Takata, R. Abe, J. Kubota and K. Domen, *Thin Solid Films*, 2011, **519**, 2087–2092.

37 J. Yao, H. Shao, H. He and Z. Fan, *Appl. Surf. Sci.*, 2007, **253**, 8911–8914.

38 K. H. Wong, C. W. Mason, S. Devaraj, J. Ouyang and P. Balaya, *ACS Appl. Mater. Interfaces*, 2014, **6**, 2679–2685.

39 H. Perron, J. Vandenborre, C. Domain, R. Drot, J. Roques, E. Simoni, J. J. Ehrhardt and H. Catalette, *Surf. Sci.*, 2007, **601**, 518–527.

40 N. Kruse and S. Chenakin, *Appl. Catal., A*, 2011, **391**, 367–376.

41 J. G. Yu, H. G. Yu, B. Cheng, X. J. Zhao, J. C. Yu and W. K. Ho, *J. Phys. Chem. B*, 2003, **107**, 13871–13879.

42 R. Liu, Z. Zheng, J. Spurgeon and X. Yang, *Energy Environ. Sci.*, 2014, **7**, 2504–2517.

43 X. Li, P. S. Bassi, P. P. Boix, Y. Fang and L. H. Wong, *ACS Appl. Mater. Interfaces*, 2015, **7**, 16960–16966.